The Scaling of the Effective Band Gaps in Indium–Arsenide Quantum Dots and Wires

Fudong Wang,[†,§] Heng Yu,[†,#] Sohee Jeong,[⊥,¶] Jeffrey M. Pietryga,[⊥] Jennifer A. Hollingsworth,[⊥] Patrick C. Gibbons,[‡,§] and William E. Buhro[†,§,*]

[†]Departments of Chemistry, [‡]Physics, [§]Center for Materials Innovation, Washington University, Saint Louis, Missouri 63130-4899, and [⊥]Chemistry Division, Los Alamos National Laboratory, Los Alamos, New Mexico 87545. [¶]Current address: Nanomechanical Systems Research Division, KIMM (Korea Institute of Machinery & Material), 171 Jang-dong, Yuseong-gu, Daejeon, 305-343, Korea. [#]Current address: MagArray, Inc., 450 El Escarpado, Stanford, CA 94305-8431.

ABSTRACT Colloidal InAs quantum wires having diameters in the range of 5–57 nm and narrow diameter distributions are grown from Bi nanoparticles by the solution–liquid–solid (SLS) mechanism. The diameter dependence of the effective band gaps (ΔE_gs) in the wires is determined from photoluminescence spectra and compared to the experimental results for InAs quantum dots and rods and to the predictions of various theoretical models. The ΔE_g values for InAs quantum dots and wires are found to scale linearly with inverse diameter (d^{-1}), whereas the simplest confinement models predict that ΔE_g should scale with inverse-square diameter (d^{-2}). The difference in the observed and predicted scaling dimension is attributed to conduction-band nonparabolicity induced by strong valence-band–conduction-band coupling in the narrow-gap InAs semiconductor.

KEYWORDS: InAs quantum wire · solution–liquid–solid · photoluminescence · effective band gap · quantum confinement · nonparabolicity · valence-band–conduction-band coupling

This study compares the diameter dependence of the effective band gaps in InAs quantum dots (QDs) and wires (QWs). Here the effective band gap, ΔE_g, is defined as the energy of the first excitonic transition. Simple models suggest that the QD and QW ΔE_gs should scale with the inverse square of diameter (d^{-2}), and that the ΔE_gs of QDs should exceed those of QWs having the same diameter by the ratio $\Delta E_g^{QW}/\Delta E_g^{QD} \approx 0.6$. We show experimentally and theoretically that ΔE_g for InAs QDs and QWs scales approximately with d^{-1} rather than with d^{-2}, and ascribe the reduced inverse scaling dimension to valence-band–conduction-band (VB–CB) coupling induced by the narrow band gap of InAs. Despite this difference in the ΔE_g scaling dimension, the effective band gaps in InAs QDs exceed those of the corresponding QWs by the predicted amount.

In recent years a strong interest has developed in how quantum confinement in semiconductors is influenced by the *shape* of the nanostructure, including how shape or confinement dimensionality influences the size dependence of electron–hole confinement energies.[1–20] To analyze such shape and size dependences, we have used effective-mass-approximation, particle-in-a-box (EMA-PIB) models,[9,10,17–20] which were first introduced many years ago to describe the electronic structures of semiconductor quantum wells[21–23] and QDs.[24–26] The EMA-PIB models suffer from severe oversimplifications, including assumptions of parabolic band shapes, infinite surface potential barriers, and size-independent electron and hole effective masses, and omissions of actual valence-band complexity and (often) electron and hole electrostatic interactions. More-accurate theoretical models are now available.[14,16,27–31] However, the appeal of the EMA-PIB models is that they are conceptually straightforward, they predict very transparently how quantum confinement depends upon shape, and they are readily tested by experiment to determine the limits of their usefulness.

The EMA-PIB models are readily applied to comparisons of the expected confinement effects in corresponding sets of quantum wells, QWs, QDs, and quantum rods (QRs). Particle-in-a-box expressions for calculating the kinetic confinement energies in planar quantum wells,[21–23] cylindrical QWs,[8,15,32–34] and spherical QDs[24–26] are given in eqs 1–3, where m_e^* and m_h^* are the effective masses of electrons and holes, respectively. The equations take similar form, and differ only in the coefficients on the right-hand side of the expressions. In all three cases, plots of ΔE_g *versus* d^{-2} (where d is thickness or diameter) are predicted to be linear, with QDs exhibiting the largest slopes and ΔE_g values, and quantum wells

*Address correspondence to buhro@wustl.edu.

Received for review June 10, 2008 and accepted August 07, 2008.

Published online August 22, 2008.
10.1021/nn800356z CCC: $40.75

© 2008 American Chemical Society

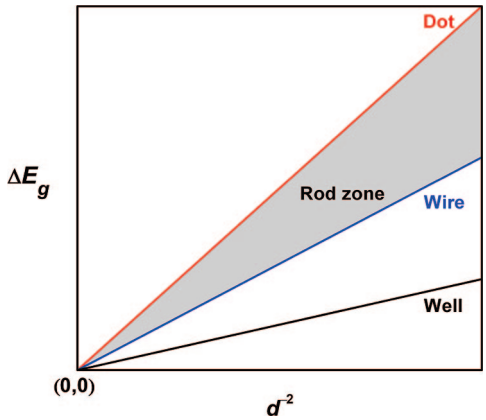

Figure 1. Slope relationships for the size dependence (d = thickness or diameter) of the effective band gaps (ΔE_gs) in quantum wells, QWs, QRs, and QDs composed of the same semiconductor material, as predicted by simple EMA−PIB models. The slope ratios are determined to be $A_{well}/A_{wire}/A_{dot}$ = 1:00:2.34:4.00. Note the rod zone bounded by the dot and wire lines.

exhibiting the smallest. The predicted slope relationships are depicted graphically in Figure 1, and the slope ratios $A_{wire}/A_{dot} = 0.585$[9,10,17] and $A_{well}/A_{wire} = 0.427$[19] are calculated from the coefficients in eqs 1−3. By a related analysis, the ΔE_g values for QRs are predicted to fall in a zone bounded by the QD and QW lines (Figure 1).[10,18]

$$\text{quantum well:} \quad \Delta E_g = \left[\frac{h^2}{8d^2}\right]\left[\frac{1}{m_e^*} + \frac{1}{m_h^*}\right] \qquad (1)$$

$$\text{quantum wire:} \quad \Delta E_g = 2.34\left[\frac{h^2}{8d^2}\right]\left[\frac{1}{m_e^*} + \frac{1}{m_h^*}\right] \qquad (2)$$

$$\text{quantum dot:} \quad \Delta E_g = 4\left[\frac{h^2}{8d^2}\right]\left[\frac{1}{m_e^*} + \frac{1}{m_h^*}\right] \qquad (3)$$

Our specific contribution has been the synthesis of various families of QWs, and a comparison of their effective band gaps to those of the corresponding QDs, quantum wells, and QRs.[9,10,17−20] These comparisons reveal that the ΔE_g values calculated by eqs 1−3 significantly overestimate experimental values when m_e* and m_h* are assigned bulk values. Indeed, EMA-PIB models are known to overestimate electron−hole confinement energies because of the deficiencies outlined above.[3,26,35−37]

However, recent experimental examples have confirmed the *relative* predictions of Figure 1. Plots of ΔE_g *versus* d^{-2} for CdSe and InP QWs and QDs have given experimental QW/QD slope ratios of A_{wire}/A_{dot}=0.53 ± 0.05[10]and 0.64 ± 0.03,[9,17] respectively, which are close to the EMA-PIB value of 0.585. Similar plots for GaAs quantum wells and QWs have given experimental A_{well}/A_{wire} slope ratios in the range of 0.41 ± 0.07 to 0.49 ± 0.09,[19] which are close to the EMA-PIB slope ratio of 0.427. Additionally, the placement of experimental ΔE_g data for CdSe and InP QRs with respect to experimental QD and QW lines in plots like Figure 1 have confirmed the predicted boundaries of the QR zone and have allowed experimental determination of the transition length at which QRs begin to exhibit the confinement behavior of QWs.[10,18] Therefore, although the *absolute* slopes predicted by eqs 1−3 are inaccurate, the slope *ratios* predicted are consistent with experimental results. The examples so far listed suggest that Figure 1 is, to a first approximation, a reasonable *comparative* picture of how quantum confinement depends on shape or the geometric dimensionality of confinement.

Because Figure 1 is only an approximate picture, due to the low level of theory employed, one may expect to find exceptions to its relative predictions. At least two such exceptions have been identified. First, we recently measured an experimental slope ratio for CdTe QWs and QDs of 1.09, near unity, which departs significantly from the EMA-PIB value of 0.585.[20] A theoretical analysis suggested that the discrepancy was due to the omission of electron−hole Coulomb interactions in eqs 2,3. The analysis further suggested that *two* regimes generally exist for such QW/QD slope-ratio comparisons: a *divergence* regime in which the slope ratios approach the EMA-PIB value, and a *convergence* regime in which the slope ratios approach unity. The convergence and divergence regimes occur above and below a threshold diameter, d_{th}, respectively, which varies with semiconductor composition. Semiconductors having small electron−hole Coulomb energies acquire large d_{th} values (≥10 nm), and thus QW-QD comparisons tend to be made in the divergence regime (slope ratio ≈ 0.6), as in the cases cited above. In contrast, semiconductors having large electron−hole Coulomb energies acquire small d_{th} values (<10 nm), and thus QW-QD comparisons are most readily made in the convergence regime (slope ratio ≈ 1.0), as in the CdTe system. Therefore, Figure 1 fails when electron−hole Coulomb energies, which are unaccounted for by the EMA-PIB models in their simplest form, become large and significant in comparison to the kinetic confinement energies.[20]

A second category of exception to Figure 1 is the prediction of the linear scaling of ΔE_g with d^{-2}, which is studied here. In the CdSe,[10] InP,[9,17] and GaAs[19] systems of quantum nanostructures discussed above, the ΔE_g-*vs*-d^{-2} data were well fit linearly; however, the lines did not extrapolate through the Figure-1 origin, as they *must* do upon relaxation of quantum confinement at large length scales. This discrepancy was investigated by our theoretical collaborators Li and Wang using density functional theory under the local-density approximation (LDA) implementing a charge-patching method and with LDA band gap corrections (CPM-LDA+C).[16] The CPM-LDA+C calculations provided ΔE_g data for quantum nanostructures of varying diameter, composition, and shape. The theoretical ΔE_g data were

fit to the empirical expression in eq 4, which yielded the scaling parameters α and β as a function of composition and shape. In general, a single value of α and a single value of β should not apply over the entire diameter range of $0 < d < \infty$.[3] However, eq 4 has proven successful over limited diameter ranges of approximately $1 < d < 20$ nm,[16] which are typical of experimental studies of quantum confinement in semiconductors. By this model ΔE_g scales linearly with $d^{-\alpha}$, where the α values are found to be in the range of *ca.* $1 < \alpha < 2$, rather than 2.[16] The origins of such differences in the scaling dimension are analyzed in this study.

$$\Delta E_g = \beta d^{-\alpha} \quad (4)$$

The linear fits to the experimental ΔE_g-*vs*-d^{-2} data do not extrapolate through the Figure-1 origin because the α values are not precisely equal to 2. Thus, plotting the ΔE_g data *versus* d^{-2}, when the actual scaling is to α values *below* 2, produces gentle curves that intersect the origin as they must.[9,10,17,19] For the CdSe, InP, GaAs, and CdTe systems referenced above, the curvature was sufficiently gentle that linear fits were possible over the limited diameter ranges studied, allowing the analyses described above. However, in the InAs system studied here, the curvature in the ΔE_g-*vs*-d^{-2} data is so severe that linear fitting of ΔE_g to the inverse-square diameter becomes impossible.

We show herein that the departure from d^{-2} scaling is a result of band nonparabolicity, particularly in the conduction band. Curvature in the ΔE_g-*vs*-d^{-2} data is always present because the band shapes are not actually parabolic as they are assumed to be by the EMA-PIB models. This curvature is less severe for quantum nanostructures having comparatively large band gaps. However, band nonparabolicity is increased in quantum nanostructures derived from small-gap semiconductors like InAs, because of a higher degree VB−CB mixing,[28,29] which induces α values that deviate more significantly from 2 toward lower values. Even so, for QW−QD comparisons made in the divergence regime, the QW/QD slope ratios remain near the EMA-PIB value of ~0.6, at the reduced scaling dimension $d^{-\alpha}$ appropriate to the specific case. Therefore the QW−QD slope-ratio prediction of Figure 1 appears to be a surprisingly general approximation.

RESULTS

Synthesis. Fanfair and Korgel previously reported the solution−liquid−solid (SLS)[38,39] growth of InAs nanowires from Bi nanoparticles using the general strategy employed here.[40] However, nanowire diameter and diameter-distribution control, and the spectroscopic properties of the nanowires were not addressed. We found that the selection of precursors, ligands, and metal-catalyst nanoparticles played an important role in the diameter-controlled SLS growth of InAs nanowires. Initial efforts resulting in nonoptimal QW growth are described in the Supporting Information.

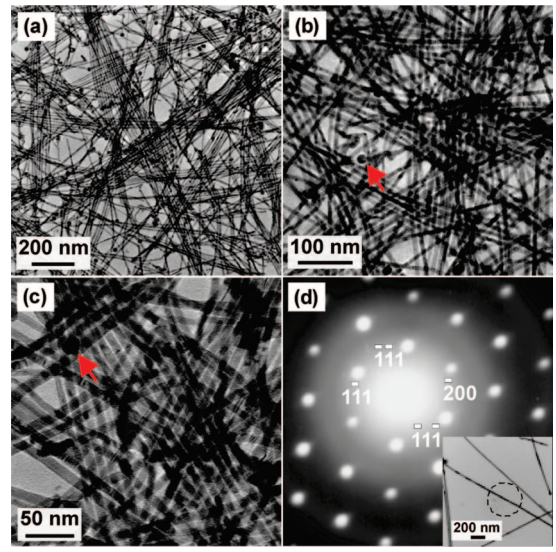

Figure 2. TEM images of InAs QWs grown from Bi nanoparticles in the presence of HDA: (a−c) 8.8 nm diameter wires having a diameter distribution of ±11%. The red arrows indicate the Bi-catalyst tips. (d) Electron-diffraction pattern in an 011 zone from the QW shown. The observed reflections are indexed, demonstrating the 111 orientation of the wire long axis. The measured (and theoretical, ICDD-PDF file 00−015−0869) *d* spacings are: 111, 0.346 ± 0.005 nm (0.350 nm); 200, 0.299 ± 0.005 nm (0.303 nm); 220, 0.214 ± 0.005 nm (0.214 nm).

High-quality InAs QWs were grown from Bi nanoparticles in the presence of *n*-hexadecylamine (HDA) (eq 5). As shown in Figure 2, narrow QW diameter distributions, a high degree of QW straightness, and excellent QW crystallinity were achieved. The amounts of reagents used, however, were quite influential to the quality of wires. The optimal $In(myr)_3/As(SiMe_3)_3$ ratio was 1.6−2.1 (see Table S1, Supporting Information). The optimal HDA/$In(myr)_3$ ratio was 6.9−8.4 for growing thin wires ($d < 10$ nm) and 4.1−4.8 for growing thick wires ($d > 10$ nm). Other ratios not in the above ranges generated kinks, broad diameter distributions, and other nonwire morphologies. Addition of tri-*n*-octylphosphine (TOP) was useful to improve the straightness and diameter distributions for thin wires, in which kinks occurred more frequently. Lower concentrations of Bi nanoparticles should be used to grow thin wires because the small Bi nanoparticles employed had a high tendency to agglomerate. The high agglomeration tendency also required reaction temperatures at the lower end of the indicated range (eq 5) for successful growth of thinner wires.

$$In(myr)_3 + As(SiMe_3)_3 \xrightarrow[\text{Bi nanoparticles}\ \text{HDA, (TOP)}]{240-335\ ^\circ C,\ \text{polydecene solvent}} \text{InAs QWs} \quad (5)$$

X-ray powder diffraction (XRD) patterns of the InAs nanowires revealed the zinc-blende structure of bulk

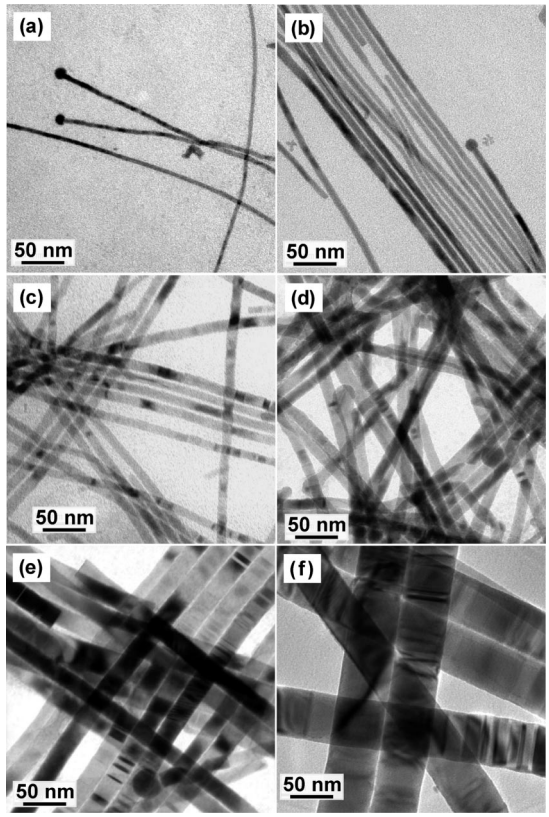

Figure 3. Representative TEM images of InAs QWs having various diameters (mean diameter ± 1 standard deviation in the diameter distribution, expressed as a percentage of the mean diameter). (a) 5.2 nm ± 13%, (b) 7.3 nm ± 19%, (c) 9.7 nm ± 15%, (d) 13.6 nm ± 12%, (e) 22.8 nm ± 15%, and (f) 57.0 nm ± 19%.

InAs (Figure S3a, Supporting Information). Energy dispersive X-ray spectroscopy (EDX) indicated an average composition of In/As ≈ (50 ± 1)/(50 ± 1) (Figure S3b). The selected-area electron diffraction (SAED) pattern in the 011 zone is shown in Figure 2d. Indexing of the reflections established the {111} close-packed crystallographic planes were oriented perpendicular the wire long axis, indicating the 111 growth direction.

Representative TEM images of InAs QWs of various diameters are shown in Figure 3. The wires were uniform along the growth direction and approached single-crystal character, although twinning defects (stacking faults) and kinks were observed (see below). Stacking faults were more evident in the thicker wires. Kinks were more evident in thinner wires. The wires were generally longer than 1 μm and up to 10 μm in length, and had diameters in the range of 5−57 nm, with standard deviations in the diameter distributions of 11−19% of the mean diameters, indicating that the nanowire diameter approached monodispersity. The diameter-distribution histograms are shown in Supporting Information, Figures S4−5.

The diameters of the wires were dependent on the diameters of Bi nanoparticles employed. The Bi-nanoparticle-diameter (d_{Bi}) dependence of the InAs nanowire diameters (d_{wire}) was empirically fit to eq 6

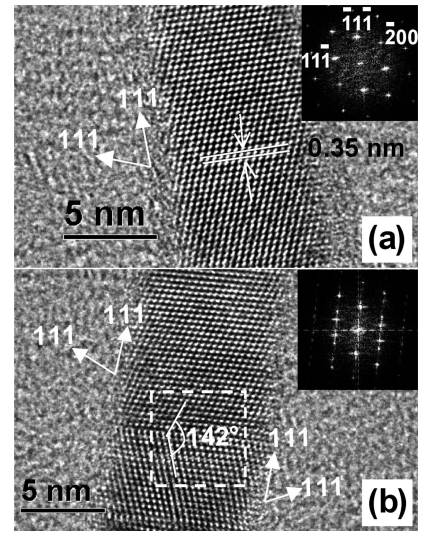

Figure 4. Representative HRTEM images of 7-nm-diameter InAs QWs viewed in a 011 zone axis. (a) The measured d_{111} lattice spacing of 0.35 nm indexed to the zinc-blende structure of bulk InAs (d_{111} = 0.3498 nm); (inset) a fast Fourier transform (FFT) of the image, indicating the wire long axis was oriented in the 111 direction. (b) The {111} twin plane oriented perpendicular to the 111 growth direction; (inset) a FFT of the image collected in the area indicated by the dashed square.

(Supporting Information, Figure S6). Thus, the diameters of the wires were almost half of the initial diameters of the Bi nanoparticles employed. We have previously interpreted nonzero intercepts like that in eq 6 (1.59 nm) to indicate initial swelling of the Bi nanoparticles by dissolution of semiconductor constituents prior to the achievement of a level of supersaturation necessary to induce QW nucleation and subsequent growth.[39]

$$d_{wire}[\text{nm}] = (0.43 \pm 0.01)d_{Bi} + (1.59 \pm 0.19)\ [\text{nm}] \quad (6)$$

Figure 4 shows high-resolution (HR) TEM images of 7 nm diameter InAs wires viewed in a 011 zone axis. A (111) twin boundary is evident in Figure 4b, in which a 180° rotation of the lattice occurs as revealed by a 142° angle between the lattice fringes on opposite sides of the boundary. HRTEM images of 5 and 20 nm diameter wires are shown in Supporting Information, Figure S7. Twinning occurred more frequently in thicker wires, consistent with the observation from Korgel and coworkers.[41] The high frequency of twin formation in the thicker wires might be attributed to the higher temperatures employed in their growth.[42]

To investigate which ligands passivated the InAs QWs, the QWs were purified and digested, and the ligands were recovered (see the Experimental Details section) and analyzed by electrospray ionization-mass spectrometry (ESI MS). Only HDA (m/z = 242.3, positive-mode) was detected by the ESI MS (Supporting Information, Figure S8). Myristate (m/z = 229.3, positive-mode; 227.3, negative mode) was not detected. Therefore, InAs QWs were passivated only by HDA.

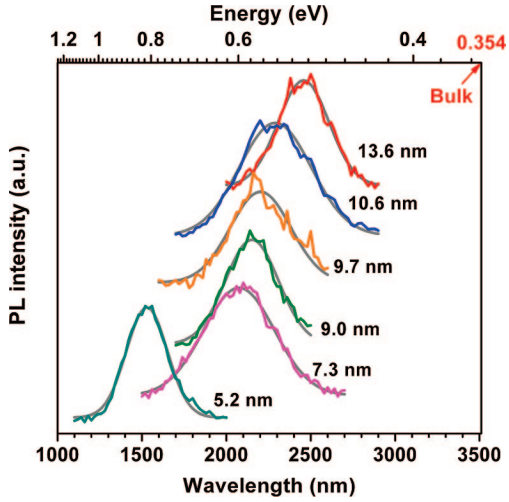

Figure 5. PL spectra for InAs QWs of various diameters. The Gaussian fits to these spectra are shown in gray. The position of the bulk InAs band gap is indicated by the red arrow.

Photoluminescence Spectroscopy and Diameter Dependence of the InAs QW Band Gap. The absorption spectra of the InAs QW specimens did not exhibit well-resolved excitonic features for all diameters studied (Supporting Information, Figure S9). Fortunately, the QWs exhibited room-temperature PL (Figure 5). As expected, the emission features red-shifted with increasing QW diameter. The features were broader than those produced by the best QD samples,[43,44] presumably because of the broader diameter distributions in the QW specimens. However, the peaks were well fit by Gaussian line shapes (shown in gray), allowing determination of the peak centers, which were taken as the energies of the first excitonic transitions in the QWs. These energies were used to calculate the effective band gaps of the QWs, that is, the confinement-induced increases over the bulk band gap (the ΔE_g values in Table 1).

The QW ΔE_g values were plotted *versus* diameter (Figure 6a), along with the corresponding data for InAs QDs. The QD data were taken from the PL spectra reported by Alivisatos and co-workers,[43] and the scanning-tunneling-microscopy (STM) measurements of Banin and co-workers.[45] These experimental data are compared in Figure 6 to the theoretical results of Li and Wang,[16] Banin and co-workers,[11] Delerue and co-workers,[30] and Niquet and co-workers.[31] Banin's experimental data for InAs QRs[11,13] are also included, as are Zanolli's experimental data for InAs QWs.[46]

TABLE 1. Spectroscopic Data for InAs QWs

InAs QW diameter, d (nm)	PL peak (nm)	PL peak/band gap (eV)	effective band gap, ΔE_g (eV)
bulk		0.354	
13.6 ± 1.6	2457 ± 3	0.506 ± 0.001	0.152 ± 0.001
10.6 ± 1.8	2282 ± 4	0.545 ± 0.001	0.191 ± 0.001
9.7 ± 1.5	2189 ± 5	0.568 ± 0.001	0.214 ± 0.001
9.0 ± 1.0	2151 ± 3	0.578 ± 0.001	0.224 ± 0.001
7.3 ± 1.4	2075 ± 3	0.599 ± 0.001	0.245 ± 0.001
5.2 ± 0.7	1529 ± 2	0.813 ± 0.001	0.459 ± 0.001

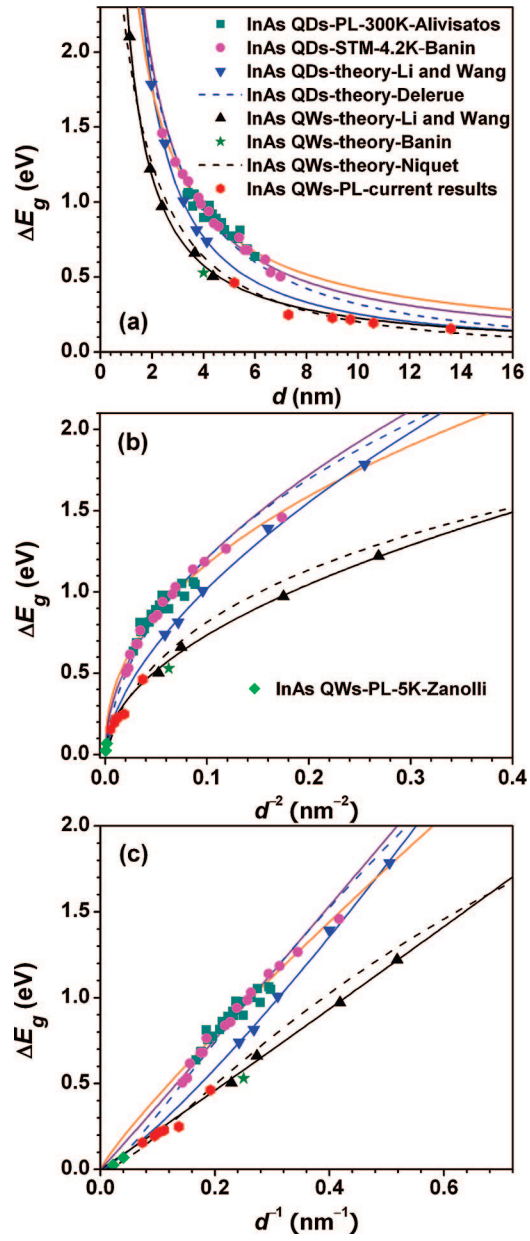

Figure 6. Effective band gap data for InAs QDs and QWs plotted as: (a) ΔE_g *vs* d; (b) ΔE_g *vs* d^{-2}; (c) ΔE_g *vs* d^{-1}. The orange, blue, and black curves are least-squares fits to the experimental QD (dark cyan squares[43] and pink circles[45]), theoretical QD (blue triangles[16]), and theoretical QW (black triangles[16]) data, respectively. The green star is the theoretical QW having an infinite length and a diameter of 4 nm.[11] The red hexagons are the current experimental QW data. The light green diamonds are experimental data for QWs of 25 and 45-nm diameters.[46] The fitting equations are ΔE_g(exp QD) = $3.23d^{-0.88}$, ΔE_g(theor QD) = $4.11d^{-1.21}$, and ΔE_g(theor QW) = $2.38d^{-1.02}$. The purple curve is the fit to the experimental QDs using the theoretical QW $d^{-1.02}$ scaling, which yielded ΔE_g(exp QD) = $3.91d^{-1.02}$. The blue dashed curve and the black dashed curve are additional theoretical predictions for QDs[30] and QWs,[31] respectively.

As noted in the Introduction, the overly simple EMA-PIB model predicts that ΔE_g values for QDs and QWs should scale linearly with the inverse square of the di-

ameter (d^{-2}).[9,10,17−19] Higher-level CPM-LDA+C calculations indicate that ΔE_g scales with $d^{-\alpha}$ where α has values in the range of ~1 to 2, which are composition and confinement-geometry dependent.[16] Thus plots of ΔE_g *versus* d^{-2} for QDs and QWs using experimental or theoretical data often contain gentle curvature because α is not precisely 2.[9,10,17−19] Even so, experimental and theoretical data for QDs and QWs plotted as ΔE_g *versus* d^{-2} have been reasonably well fit linearly, *over limited diameter ranges*, which has allowed several useful comparisons based on the slopes of the fits.[9,10,17−19]

The data for InAs QDs and QWs are exceptional (to date), because they cannot be practically analyzed using the d^{-2} scaling. The α value for InAs QWs is 1.02, which is among the lowest known. Consequently, the ΔE_g-*vs*-d^{-2} plot using the CPM-LDA+C theoretical data for InAs QWs is markedly nonlinear (Figure 6b). As the diameter ranges for the experimental and theoretical QW data do not overlap, we believe it most appropriate to plot the combined data on a common curve. Furthermore, the theoretical data for InAs QDs produce $\alpha = 1.21$, whereas the experimental data for InAs QDs are best fit with $\alpha = 0.88$. Thus, the best compromise scaling for comparing all of the theoretical and experimental QD and QW data is ΔE_g *vs* d^{-1}.

Accordingly, Figure 6c plots the ΔE_g values for InAs QDs and QWs *vs* d^{-1}. The CPM-LDA+C theoretical and experimental QW data are in excellent agreement as all points fall on the same (black) curve, which is nearly linear ($\alpha = 1.02$) at the d^{-1} scaling. A separate theoretical curve for QWs (black dashes in Figure 6) was proposed by Niquet, Delerue, and co-workers,[31] who used a different empirical fitting function than that employed for the CPM-LDA+C data (eq 4).[16] The theoretical predictions of the two methods are quite similar (see Figure 6c).

The CPM-LDA+C theoretical and experimental QD data do not agree as closely, and show curvature in opposite directions (Figure 6c), as indicated by the fitted α values given above. The blue and orange curves are the fits to the CPM-LDA+C theoretical and experimental QD data, respectively. Although the Delerue−Niquet theoretical curve[30] (blue dashes in Figure 6) provides a better fit to experimental QD data, the CPM-LDA+C results are employed for the comparisons in this study. Note that the QW data lie below the QD data, consistent with expectation that 2D confinement in wires is weaker than 3D confinement in dots. The *quantitative* difference in the QW and QD data is analyzed next.

The EMA-PIB model predicts a slope ratio $A_{wire}/A_{dot} = 0.585$ in plots of ΔE_g *versus* d^{-2} for sets of QWs and QDs composed of the same semiconductor material. However, as revealed in Figure 6c, the ΔE_g data for InAs QDs and QWs are nearly linear with respect to d^{-1} rather than d^{-2}. Consequently, we sought to calculate a QW-QD slope ratio by a common scaling with α near one. As indicated above, the experimental and theoretical data for InAs QWs were well fit with $\alpha = 1.02$. The average of the experimental ($\alpha = 0.88$) and theoretical values ($\alpha = 1.21$) for InAs QDs was $\alpha = 1.04$, essentially identical to the QW value. Therefore, we refit the experimental QD data with respect to $d^{-1.02}$ ($\alpha = 1.02$; purple curve in Figure 6c) for direct comparison to the fitting results for QWs. The slope ratio was thus $\beta_{wire}/\beta_{dot} = 2.38/3.91 = 0.609$, very close to the value predicted by the EMA-PIB model (for the d^{-2} scaling). The similarity of these values will be analyzed in the Discussion.

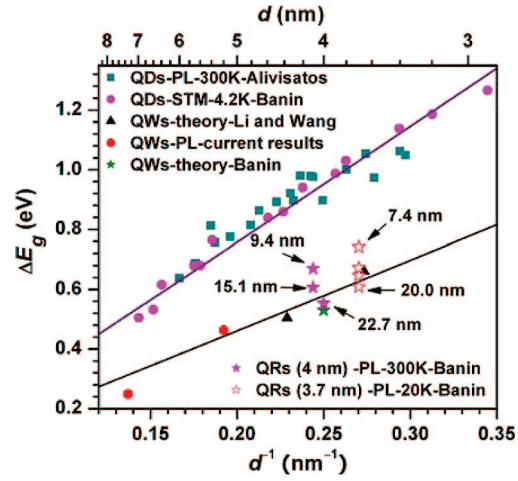

Figure 7. Effective band gap data for InAs QRs plotted as ΔE_g *vs* d^{-1} in comparison with the QD and QW values. The ~4 nm diameter QRs (pink stars), and 3.7 nm diameter QRs (empty red stars) were taken from refs 11 and 13, respectively. The lengths for some QRs are marked.

We also plotted literature InAs QR data[11,13] *versus* d^{-1} in Figure 7. The experimental curves for QDs and QWs from Figure 6c are replotted in Figure 7 to provide the boundaries of the expected QR zone, within which the QR ΔE_g values should appear. As expected, the QR values fell within or close to the QR zone. The ΔE_g values for the shorter QRs were well inside the zone, whereas the values for the longer QRs were on or below the QW curve, suggesting that the long QRs had achieved the 2D confinement of QWs. The length (~20 nm) at which the QR to QW transition apparently occurred was somewhat shorter than expected by comparison to the bulk exciton Bohr radius for InAs of 35 nm. QRs shorter than 35 nm should be still confined in the third, length dimension. Additional theoretical study or experimental band gap data for QWs having diameters in the range of 2−5 nm will be necessary to clearly define the QR−QW transition length in the InAs system.

DISCUSSION

A primary purpose of this study, and related studies in this series,[9,10,17,19,20] has been to establish how the size dependences of the confinement energies, the ΔE_gs, should compare in corresponding sets of QWs and QDs. As noted above, the overly simple EMA-PIB model predicts that plots of ΔE_g *versus* d^{-2} for QWs and

QDs should be linear and exhibit a slope ratio $A_{wire}/A_{dot} = 0.585$. However, in general the ΔE_g values do not scale linearly with d^{-2}, and for the InAs QDs and QWs compared here a nearly linear scaling is achieved with ΔE_g *versus* d^{-1}. Thus a new question arises: what should the QW/QD slope ratio be at the d^{-1} scaling used here, or other at scalings that may be more appropriate in QW-QD comparisons for other semiconductor systems?

Therefore, we now calculate a theoretical QW/QD slope ratio appropriate for the $d^{-\alpha}$ scaling employed in the present comparison. This ratio is calculated using Li and Wang's theoretical data for InAs QDs and QWs determined by CPM-LDA+C.[16] We reiterate that in general a single value of α should not apply over the entire diameter range of $0 < d < \infty$,[3] but a single α successfully describes the diameter dependence of ΔE_g (by eq 4) over limited, relevant diameter ranges of approximately $1 < d < 20$ nm.[16] Equation 4 should not be used to extrapolate ΔE_g values outside this limited range.

The QD and QW data are separately fit according to eq 4, yielding $\alpha_{dot} = 1.21$, $\beta_{dot} = 4.11$, $\alpha_{wire} = 1.02$, and $\beta_{wire} = 2.38$. The theoretical QW/QD slope ratio would thus be β_{wire}/β_{dot}; however, the β values used must be calculated at the same value of α. The fitted α_{dot} and α_{wire} values differ slightly, and so a common value must be chosen. Li and Wang's convention[14] is to use the α_{dot} value, and so to refit the QW data according to eq 4 using α_{dot}, thereby obtaining a new β'_{wire} value. By that convention, we calculate a theoretical QW/QD slope ratio of $\beta'_{wire}/\beta_{dot} = 0.625$. Alternatively, both the QD and QW data could be refit to an average value of $\alpha = 1.11$. Using that procedure, we calculate a theoretical QW/QD slope ratio of $\beta'_{wire}/\beta'_{dot} = 0.657$. A final option is to refit the QD data using α_{wire}, and thus obtain a $\beta_{wire}/\beta'_{dot} = 0.690$ at a common $\alpha = 1.02$. Therefore, the theoretical QW/QD slope ratio is within 0.62−0.69, and the experimental value of 0.61 (determined above) falls very close to this range. All of these values are near the EMA-PIB slope ratio of 0.585.

Li and Wang have previously calculated $\beta'_{wire}/\beta_{dot}$ (QW/QD) slope ratios for various QW−QD compositions having α_{dot} values ranging from 1.02−1.69.[16] With an important exception (see below), the theoretical QW/QD slope ratios were in the range of 0.495−0.676 at the various optimal $d^{-\alpha}$ scalings employed. As noted by Li and Wang and in the discussion above, this range is remarkably consistent with the EMA-PIB slope ratio of 0.585. Their theoretical finding, that QW/QD slope ratios are 0.6 ± 0.1 even for α values considerably smaller than 2, is supported by the experimental results of this study. Therefore, despite the general inadequacy of the d^{-2} scaling at small diameters, the EMA-PIB QW/QD slope-ratio prediction appears to be a surprisingly robust approximation, for QD−QW comparisons made in the *divergence* regime.

As noted in the Introduction, deviations from QW/QD slope ratios of ~0.6 occur in the *convergence* regime, at diameters *greater* than a threshold diameter, d_{th}, which varies from semiconductor to semiconductor.[20] At diameters above d_{th}, the slope ratio tends toward unity (1.0), as QD and QW effective band gaps converge to similar values (at equal QW and QD diameters). As previously indicated, semiconductors having large electron−hole Coulomb energies tend to have small d_{th} values (<10 nm), and so QW/QD slope-ratio determinations are most readily made in the convergence regime. Therefore, Li and Wang reported a theoretical $\beta'_{wire}/\beta_{dot}$ slope ratio 0.971 for AlN QWs and QDs.[16] Furthermore, we measured an experimental QW/QD slope ratio of 1.09 for CdTe QWs and QDs.[20] Both AlN and CdTe have relatively large Coulomb energies (the calculated bulk exciton binding energies are 42.5 and 10.7 meV, respectively). We have previously argued that QW−QD effective-band gap convergence in such cases is enforced by comparatively larger Coulomb interactions in QDs than in QWs having synthetically relevant capping ligands.[20]

In contrast, semiconductors with small Coulomb energies have larger d_{th} values (≥10 nm), and QW/QD slope ratios are thus obtained in the divergence regime (slope ratio ≈ 0.6). *Bulk* InAs has a small Coulomb energy of 1.5 meV (calculated bulk exciton binding energy).[3] Correspondingly, we estimate the exciton binding energies for InAs QWs having diameters in our range of 5−14 nm to be 14−13 meV, respectively, using the method of Shabaev and Efros;[15] these binding energies are only 8−3%, respectively, of the ΔE_gs of the QWs (see Supporting Information). Similarly, The exciton binding energies for InAs QDs having diameters in the range of 2−7 nm (see Figure 6) are estimated to be 170−48 meV, respectively, using Brus's method;[26] these binding energies are only 10−8%, respectively, of the ΔE_gs of the QDs (see Supporting Information). The calculated d_{th} value for InAs is 17.7 nm,[20] consistent with its small Coulomb energy. Therefore, we measured an experimental slope ratio of 0.61, within the divergence regime for this system.

We now consider why the ΔE_g scaling for InAs QDs and QWs departs so significantly from the d^{-2} scaling predicted by the EMA-PIB model. The exciton binding (electron−hole Coulomb) energies in InAs QDs and QWs make relatively small contributions to the ΔE_gs and can be neglected, as rationalized above. The confinement of the electron in InAs QDs and QWs makes the dominant contribution to ΔE_g. (The component of the bulk InAs exciton Bohr radius assigned to the electron is 33.6 nm, whereas that assigned to the heavy hole is 2.1 nm;[3] hence the electron is more strongly confined.) Therefore, this discussion will focus on the shape of the electron (conduction) band, and its effect on ΔE_g. The EMA-PIB model assumes a parabolic electron band in k space (Figure 8a), for which the ΔE_g scaling is

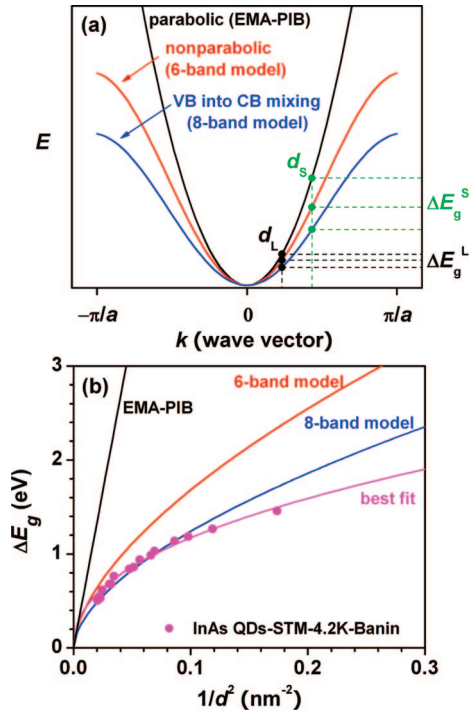

Figure 8. Comparison of different models used for the calculation of (a) electron band structure in *k* space and (b) ΔE_g *vs* d^{-2} for InAs QDs. The comparison of the band structures from different models in panel a is made qualitatively. ΔE_g^S and ΔE_g^L represent ΔE_g at small *d* (d_S) and large *d* (d_L), respectively. The curves for the EMA−PIB model in panel b are calculated using bulk effective masses of the electron and heavy hole[58] and the curves for the 6-band and 8-band models in panel b are taken from ref 59. The pink circles are experimental data for InAs QDs taken from ref 45.

precisely d^{-2} (Figure 8b).[24] However, the parabolic shape is a fair approximation only near $k = 0$; that is, near the bottom of the band. Quantum confinement raises the energy of the first quantized level above the bottom of the band, to nonzero values of *k*. As *d* decreases, the position of the first quantized level shifts to progressively larger absolute values of *k* and thus to higher energies in the band, where the band shape deviates from parabolic toward lower energy (Figure 8a).[28,29] This nonparabolicity may be described by assigning a diameter (or energy) dependence to the electron effective mass (m_e*), such that m_e* increases as *d* decreases.[47−56] Therefore, the confinement energy ΔE_g increases more slowly with decreasing *d* than predicted by the parabolic band shape of the EMA-PIB model (Figure 8a), imparting downward curvature to the ΔE_g-*vs*-d^{-2} plot (Figure 8b),[29] which is better fit by an α value of less than 2.

Even though the α values for QDs and QWs of a wide range of compositions are less than 2,[16,20] the experimental ΔE_g-*vs*-d^{-2} data have conformed fairly closely to linear fits over the limited diameter ranges of our prior studies, for InP, CdSe, and CdTe QDs and QWs. That is because the curvature in the data has been reasonably gentle, reflecting α values significantly greater than 1. In the case of InAs, however, the deviation from linearity is so severe, and the α values so low, that linear fitting is no longer possible. An additional component to the deviation from electron-band parabolicity is present in this case.

InAs is a narrow-gap semiconductor, for which VB−CB coupling in quantum nanostructures has a significant influence on the shape of the electron band (i.e., conduction band). Ekimov, Efros and co-workers,[27] and Efros and Rosen[29] have developed 6-band and 8-band theoretical models to describe cases for which VB−CB coupling *are not*, and *are* important, respectively. The 6-band model, which considers mixing of the valence bands with one another only, is best applied to quantum nanostructures derived from comparatively wide-gap semiconductors such as CdS and CdSe, where the electron band behaves essentially independently.[29] However, quantum nanostructures derived from narrow-gap semiconductors such as PbS, PbSe,[28] and InAs[29] are better described by an 8-band[29] or related models,[28,57] which explicitly consider the significant mixing of valence-band character into the electron band (and vice versa).

Figure 8 reveals the effects of VB−CB coupling that are important to this discussion. The mixing of valence-band character into the electron band induces a greater nonparabolicity in this band than is present in quantum nanostructures derived from wider-gap semiconductors (Figure 8a).[28,29,57]This in turn results in a more severe downward curvature in the ΔE_g-*vs*-d^{-2} plot. Figure 8b compares a ΔE_g-*vs*-d^{-2} plot for InAs QDs derived from experimental data[45] to the predictions of the EMA-PIB, 6-band, and 8-band models.[59] The 8-band model, which mixes valence-band character into the electron band and induces the greatest deviation from the d^{-2} scaling, obviously corresponds most closely to the experimental data.[59]

The magnitude of VB−CB coupling is approximated by eq 7, where E_g is the bulk band gap and *C* is a coupling constant that takes values in the range of 0 (no coupling) to 1 (maximum coupling).[29] Values of *C* for 5-nm-diameter QDs and QWs composed of various semiconductors are recorded in Table 2. For the comparatively wide-gap semiconductors CdSe, CdTe, GaAs, and InP, *C* ranges from 0.31−0.48. We have succeeded in making slope-ratio comparisons using the d^{-2} scaling for these systems.[9,10,17,19,20] In contrast, the *C* values for InAs QDs and QWs are 0.83 and 0.75, respectively. At these larger values, the VB−CB coupling is sufficiently strong that the d^{-2} scaling fails, and a lower value of α must be used. Thus we may anticipate a similar failure of the d^{-2} scaling for other QD−QW comparisons involving narrow-gap semiconductors.

$$C = \left[\frac{\Delta E_g}{E_g + \Delta E_g}\right]^{\frac{1}{2}} \quad (7)$$

TABLE 2. VB−CB Coupling Constant (*C*) for QDs and QWs

		C[a]	
semiconductor (d = 5 nm)	Band gap, [58] E_g (eV, 300 K)	QD	QW
InAs	0.354	0.83	0.75
InP	1.35	0.48	0.40
GaAs	1.43	–	0.44
CdTe	1.49	0.44	0.44
CdSe	1.75	0.36	0.31

[a]Calculated from eq 7 according to ref 29. ΔE_gs for InAs QDs and QWs are extrapolated from $\Delta E_g(\text{exp QD}) = 3.23d^{-0.88}$ and $\Delta E_g(\text{theor QW}) = 2.38d^{-1.02}$, respectively (see Figure 6 for details). ΔE_gs for InP,[17] GaAs,[19] CdTe,[20] and CdSe[10] QDs and QWs are extrapolated from the ΔE_g-*vs*-d^{-2} plots using published experimental data.

CONCLUSION

The overly simple EMA-PIB model asserts that the electron−hole confinement energies in QDs and QWs should scale with the inverse-square of the diameter, and that the QW−QD slope ratio from the ΔE_g-*vs*-d^{-2} plots should be 0.6. Neither of these approximations is universally valid. First, our prior study in the CdTe system established that in cases of comparatively high electron−hole Coulomb energies, quantum-confined QD and QW band gaps may be contained within a *convergence* diameter regime for which QW−QD slope ratios approach unity rather than 0.6.[20] Second, in all cases, ΔE_g actually scales with $d^{-\alpha}$ over limited, relevant diameter ranges, where α is in the range of 1−2, but is always <2. Even so, for QD−QW comparisons within the band gap *divergence* regime, at diameters below a threshold value d_{th} that varies with the semiconductor, the QW/QD slope ratios are in the range of 0.5−0.7, irrespective of the precise value of α. This range is notably consistent with the approximate value of 0.6 calculated by the EMA-PIB model. We showed here that departure from the approximate d^{-2} scaling is especially pronounced in QDs and QWs of narrow-gap semiconductors, for which the shape of the electron band deviates most severely from the parabolic approximation.[28,29,57]

EXPERIMENTAL DETAILS

Materials. The precursor tris(trimethylsilyl)arsine ($As(SiMe_3)_3$) was prepared by a literature method.[60] Stock solutions of $As(SiMe_3)_3$ (containing 0.30−0.33 mmol $As(SiMe_3)_3$/mL polydecene) were prepared and stored in a refrigerator for later use. Stock solutions of Bi-catalyst nanoparticles (containing 0.04 mmol Bi atoms/g solution, if not specifically mentioned otherwise) were prepared as described previously.[61] Preparation of indium myristate ($In(myr)_3$) and a stock solution of it was described previously.[17] Myristic acid (99.5%), tri-*n*-octylphosphine (TOP, 90%), *n*-hexadecylamine (HDA, 90%), and hydrogenated poly(1-decene) were purchased from Aldrich. HDA was vacuum distilled at 200 °C. The other reagents were used as received.

Synthesis of InAs QWs. All synthetic steps were conducted under dry, O_2-free N_2(g), but the isolation and purification steps were conducted in the ambient atmosphere. The quantities of reagents used are recorded in Table S1 (Supporting Information). In a typical preparation, $In(myr)_3$ stock solution (1.81 g, 0.27 mmol of In), HDA (550 mg, 2.28 mmol), TOP (in some experiments), and polydecene (3 g) were loaded into a Schlenk reaction tube. In a separate vial, the Bi nanoparticle solution (40−80 mg, 0.0016−0.0032 mmol of Bi atoms) was diluted with polydecene to 0.5 mL, and the vial was septum capped. The $As(SiMe_3)_3$ stock solution (0.5 mL, 0.15−0.17 mmol of $As(SiMe_3)_3$) and the Bi particle stock solution were loaded into the same 3 mL syringe. The reaction mixture in the Schlenk tube was degassed under vacuum (10^{-3} torr) at ~100 °C for 5 min, and then inserted into a preheated salt bath ($NaNO_3/KNO_3$, 46:54 by weight), held at a desired temperature (240−335 °C; see Supporting Information, Table S1). The reaction tube was allowed to equilibrate for 1−2 min, and then the $As(SiMe_3)_3$ and Bi nanoparticle mixture was quickly injected into the reaction tube. The color of the reaction mixture immediately turned red and finally to grayish brown. The reaction tube was withdrawn from the bath at 5 min after the injection and allowed to cool to room temperature. Black precipitates were observed in the mixtures, which were shown to be the InAs QWs. Alternatively, the $As(SiMe_3)_3$ stock solution could be injected first to produce a deep red solution and then followed 0.5−1 min later by the injection of the Bi stock solution (see Table S1 for details), which generally resulted in better control over diameter distributions and QW straightness.

A small portion of the solidified reaction mixture was taken and the black InAs QW precipitate was isolated by adding toluene (*ca.* 5 mL) and isopropyl alcohol (*ca.* 2 mL) to the mixture, followed by centrifugation (benchtop centrifuge) and decanting of the supernatant. The QWs were purified by redispersion in a mixture of toluene (*ca.* 4 mL) and isopropyl alcohol (*ca.* 2 mL) upon sonication in a cleaning bath, followed by centrifugation and decanting of the supernatant. Two such redispersion-centrifugation purification cycles were generally sufficient to prepare QW specimens for absorption and emission spectroscopic and TEM analyses. After purification the InAs QWs were redispersed in carbon tetrachloride (CCl_4) (or toluene) upon sonication to form uniform and optically clear light-brown solutions for spectroscopic (or TEM) analyses. After a few hours the QWs began to precipitate from the CCl_4 or toluene dispersions; however, they were easily redispersed by gentle shaking. HRTEM imaging showed that there was no noticeable change in the surface oxide layer 3 weeks after the purification.

Recovery and Characterization of Ligands on the Surface of InAs QWs. The method employed was adapted from Peng and coworkers.[62] The as-prepared wires were isolated from the solidified reaction mixture by adding toluene (*ca.* 5 mL) and isopropyl alcohol (*ca.* 5 mL) and collected by centrifugation as described above. The redispersion-centrifugation purification cycle was repeated three times to the isolated wires to ensure that all free ligands were removed. The powder containing the purified wires was digested by HCl. The organic ligands were extracted into chloroform and the chloroform layer was isolated and subsequently vaccuum-dried. The organic ligands were extracted by methanol and analyzed by electrospray-ionization mass spectrometry (ESI-MS) on Q-TOF using CH_3CN/H_2O (50/50, v/v) as the solvent, by the Washington University Mass Spectrometry Resource.

Optical Spectroscopy. The InAs QWs were precipitated and purified as described above. The wires were redispersed in CCl_4 for the spectroscopic analysis. Absorption spectra were taken using a Perkin-Elmer Lamda 950 UV−vis−NIR spectrometer. The PL spectra were collected using a home-built computer-controlled spectrometer with a liquid-nitrogen-cooled InSb detector, from dilute samples in CCl_4, excited by an 808 nm diode laser chopped at 3 kHz.

Transmission Electron Microscopy (TEM). All of the samples were purified by isopropyl alcohol/toluene precipitation from the reaction solution as described above. Carbon-coated copper grids were dipped in the toluene solution and then immediately taken out to evaporate the solvent. TEM images and energy-dispersive

X-ray analysis (EDX) of InAs nanowires were collected using a JEOL 2000 FX microscope with an acceleration voltage of 200 kV. Selected-area electron-diffraction (SAED) patterns were taken with a camera length of 120 cm. The diameter statistics for the wire samples were measured by a commercial software-Image Pro Progress (version 4.5) at the 2× zoom from 200−600 wires in TEM images taken at a magnification of 500K×, and expressed as the statistical mean diameter ± 1 standard deviation (Supporting Information, Table S1). High-resolution TEM (HRTEM) was carried out on a JEOL JEM-2100F TEM at 200 kV.

X-ray Powder Diffraction (XRD). XRD patterns were obtained using a Rigaku Dmax A vertical powder diffractometer with Cu Kα radiation (λ = 1.5418 Å) and Materials Data Incorporated (MDI) automation and Jade software.

Acknowledgment We thank Richard A. Loomis (Washington University), Todd D. Krauss (U. of Rochester) for helpful discussions, and Ginny Wayman for assistance with NIR absorption spectra. We are grateful for funding from the National Science Foundation (under Grant No. CHE-0518427) and the Center for Materials Innovation at Washington University. J.A.H. and S.J. were supported by LANL LDRD funds. J.M.P. was supported by an Intelligence Community Postdoctoral Research Fellowship.

Supporting Information Available: Detailed synthetic conditions and resulting size data for InAs QWs, additional TEM images of InAs QWs, an XRD pattern and EDX spectrum from InAs QWs, diameter-distribution histograms for InAs QWs, a plot of InAs QW diameter as a function of the initial Bi-catalyst-nanoparticle diameter, HRTEM images of 5 and 20 nm diameter InAs QWs, a mass spectrum of the recovered surface ligands for InAs QWs, absorption spectra for InAs QWs, and estimation of exciton binding energies for InAs QDs and QWs. This material is available free of charge *via* the Internet at http://pubs.acs.org.

REFERENCES AND NOTES

1. Kayanuma, Y. Wannier Excitons in Low-Dimensional Microstructures: Shape Dependence of the Quantum Size Effect. *Phys. Rev. B* **1991**, *44*, 13085–13088.
2. Li, L.-S; Hu, J.; Yang, W.; Alivisatos, A. P. Band Gap Variation of Size- and Shape-Controlled Colloidal CdSe Quantum Rods. *Nano Lett.* **2001**, *1*, 349–351.
3. Yoffe, A. D. Low-Dimensional Systems: Quantum Size Effects and Electronic Properties of Semiconductor Microcrystallites (Zero-Dimensional Systems) and Some Quasi-Two-Dimensional Systems. *Adv. Phys.* **2002**, *51*, 799–890.
4. Gudiksen, M. S.; Wang, J.; Lieber, C. M. Size-Dependent Photoluminescence from Single Indium Phosphide Nanowires. *J. Phys. Chem. B* **2002**, *106*, 4036–4039.
5. Katz, D.; Wizansky, T.; Millo, O.; Rothenberg, E.; Mokari, T.; Banin, U. Size-Dependent Tunneling and Optical Spectroscopy of CdSe Quantum Rods. *Phys. Rev. Lett.* **2002**, *89*, 086801.
6. Hu, J.; Wang, L.-W.; Li, L.-S.; Yang, W.; Alivisatos, A. P. Semiempirical Pseudopotential Calculation of Electronic States of CdSe Quantum Rods. *J. Phys. Chem. B* **2002**, *106*, 2447–2452.
7. Buhro, W. E.; Colvin, V. L. Semiconductor Nanocrystals: Shape Matters. *Nat. Mater.* **2003**, *2*, 138–139.
8. Li, J.; Wang, L.-W. High Energy Excitations in CdSe Quantum Rods. *Nano Lett.* **2003**, *3*, 101–105.
9. Yu, H.; Li, J.; Loomis, R. A.; Wang, L.-W; Buhro, W. E. Two-*versus* Three-Dimensional Quantum Confinement in Indium Phosphide Wires and Dots. *Nat. Mater.* **2003**, *2*, 517–520.
10. Yu, H.; Li, J.; Loomis, R. A.; Gibbons, O. C.; Wang, L.-W; Buhro, W. E. Cadmium Selenide Quantum Wires and the Transition from 3D to 2D Confinement. *J. Am. Chem. Soc.* **2003**, *125*, 16168–16169.
11. Kan, S.; Mokari, T.; Rothenberg, E.; Banin, U. Synthesis and Size-Dependent Properties of Zinc-Blende Semiconductor Quantum Rods. *Nat. Mater.* **2003**, *2*, 155–158.
12. Kan, S.; Aharoni, A.; Mokari, T.; Banin, U. Shape Control of III−V Semiconductor Nanocrystals: Synthesis and Properties of InAs Quantum Rods. *Faraday Discuss.* **2004**, *125*, 23–38.
13. Steiner, D.; Katz, D.; Millo, O.; Aharoni, A.; Kan, S.; Mokari, T.; Banin, U. Zero-Dimensional and Quasi One-Dimensional Effects in Semiconductor Nanorods. *Nano Lett.* **2004**, *4*, 1073–1077.
14. Li, J.; Wang, L.-W. Comparison between Quantum Confinement Effects of Quantum Wires and Dots. *Chem. Mater.* **2004**, *16*, 4012–4015.
15. Shabaev, A.; Efros, Al. L. 1D Exciton Spectroscopy of Semiconductor Nanorods. *Nano Lett* **2004**, *4*, 1821–1825.
16. Li, J.; Wang, L.-W. Band-Structure-Corrected Local Density Approximation Study of Semiconductor Quantum Dots and Wires. *Phys. Rev. B* **2005**, *72*, 125325.
17. Wang, F.; Yu, H.; Li, J.; Hang, Q.; Zemlyanov, D.; Gibbons, P. C.; Wang, L.-W.; Janes, D. B.; Buhro, W. E. Spectroscopic Properties of Colloidal Indium Phosphide Quantum Wires. *J. Am. Chem. Soc.* **2007**, *129*, 14327–14335.
18. Wang, F.; Buhro, W. E. Determination of the Rod-Wire Transition Length in Colloidal Indium Phosphide Quantum Rods. *J. Am. Chem. Soc.* **2007**, *129*, 14381–14387.
19. Dong, A.; Yu, H.; Wang, F.; Buhro, W. E. Colloidal GaAs Quantum Wires: Solution-Liquid-Solid Synthesis and Quantum-Confinement Studies. *J. Am. Chem. Soc.* **2008**, *130*, 5954–5961.
20. Sun, J.; Wang, L.-W.; Buhro, W. E. Synthesis of Cadmium Telluride Quantum Wires and the Similarity of Their Effective Band Gaps to Those of Equidiameter Cadmium Telluride Quantum Dots. *J. Am. Chem. Soc.* **2008**, *130*, 7997–8005.
21. Harper, P. G.; Hilder, J. A. Exciton Spectra in Thin Crystals. *Phys. Status Solidi* **1968**, *26*, 69–76.
22. Consadori, F.; Frindt, R. F. Crystal Size Effects on the Exciton Absorption Spectrum of WSe_2. *Phys. Rev. B* **1970**, *2*, 4893–4896.
23. Dingle, R. Confined Carrier Quantum States in Ultrathin Semiconductor Heterostructures. *Festkörperprobleme* **1975**, *XV*, 21–48.
24. Efros, Al. L.; Efros, A. L. Interband Absorption of Light in a Semiconductor Sphere. *Sov. Phys. Semicond.* **1982**, *16*, 772–775.
25. Rossetti, R.; Nakahara, S.; Brus, L. E. Quantum Size Effects in the Redox Potentials, Resonance Raman Spectra, and Electronic Spectra of CdS Crystallites in Aqueous Solution. *J. Chem. Phys.* **1983**, *79*, 1086–1088.
26. Brus, L. E. Electron-Electron and Electron-Hole Interactions in Small Semiconductor Crystallites: The Size Dependence of the Lowest Excited Electronic State. *J. Chem. Phys.* **1984**, *80*, 4403–4409.
27. Ekimov, A. I.; Hache, F.; Schanne-Klein, M. C.; Ricard, D.; Flytzanis, C.; Kudryavtsev, I. A.; Yazeva, T. V.; Rodina, A. V.; Efros, Al. L. Absorption and Intensity-Dependent Photoluminesence Measurements on CdSe Quantum Dots: Assignment of the First Electronic Transitions. *J. Opt. Soc. Am. B* **1993**, *10*, 100–107.
28. Kang, I.; Wise, F. W. Electronic Structure and Optical Properties of PbS and PbSe Quantum Dots. *J. Opt. Soc. Am. B* **1997**, *14*, 1632–1646.
29. Efros, Al. L.; Rosen, M. Quantum Size Level Structure of Narrow-Gap Semiconductor Nanocrystals: Effect of Band Coupling. *Phys. Rev. B* **1998**, *58*, 7120–7135.
30. Niquet, Y. M.; Delerue, C.; Allan, G. Interpretation and Theory of Tunneling Experiments on Single Nanostructures. *Phys. Rev. B* **2002**, *65*, 165334.
31. Niquet, Y. M.; Lherbier, A.; Quang, N. H.; Fernandez-Serra, M. V.; Blase, X.; Delerue, C. Electronic Structure of Semiconductor Nanowires. *Phys. Rev. B* **2006**, *73*, 165319.
32. Gold, A.; Ghazali, A. Analytical Results for Semiconductor Quantum-Well Wire: Plasmons, Shallow Impurity States, and Mobility. *Phys. Rev. B* **1990**, *41*, 7626–7640.
33. Nanda, K. K.; Kruis, F. E.; Fissan, H. Energy Levels in Embedded Semiconductor Nanoparticles and Nanowires. *Nano Lett.* **2001**, *1*, 605–611.

34. Zhao, X.; Wei, C. M.; Yang, L.; Chou, M. Y. Quantum Confinement and Electronic Properties of Silicon Nanowires. *Phys. Rev. Lett.* **2004**, *92*, 236805.
35. Wang, Y.; Suna, A.; Mahler, W.; Kasowski, R. PbS in Polymers: From Molecules to Bulk Solids. *J. Chem. Phys.* **1987**, *87*, 7315–7322.
36. Lippens, P. E.; Lannoo, M. Calculation of the Band Gap for Small CdS and ZnS Crystallites. *Phys. Rev. B* **1989**, *39*, 10935–10942.
37. Wang, Y.; Herron, N. Nanometer-Sized Semiconductor Clusters: Materials Synthesis, Quantum Size Effects, and Photophysical Properties. *J. Phys. Chem.* **1991**, *95*, 525–532.
38. Trentler, T. J.; Hichman, K. M.; Goel, S. C.; Viano, A. M.; Gibbons, P. C.; Buhro, W. E. Solution−Liquid−Solid Growth of Crystalline III−V Semiconductors: an Analogy to Vapor−Liquid−Solid Growth. *Science* **1995**, *270*, 1791–1794.
39. Wang, F.; Dong, A.; Sun, J.; Tang, R.; Yu, H.; Buhro, W. E. Solution−Liquid−Solid Growth of Semiconductor Nanowires. *Inorg. Chem.* **2006**, *45*, 7511–7521.
40. Fanfair, D. D.; Korgel, B. A. Bismuth Nanocrystal-Seeded III−V Semiconductor Nanowire Synthesis. *Cryst. Growth Des.* **2005**, *5*, 1971–1976.
41. Davidson, F. M.; Lee, D. C.; Fanfair, D. D.; Korgel, B. Lamellar Twinning in Semiconductor Nanowires. *J. Phys. Chem. C.* **2007**, *111*, 2929–2935.
42. Johansson, J.; Karlsson, L. S.; Svensson, C. P. T.; Martensson, T.; Wacaser, B. A.; Deppert, K.; Samuelson, L.; Seifert, W. Structural Properties of κB-Oriented III−V Nanowires. *Nat. Mater.* **2006**, *5*, 574–580.
43. Guzelian, A. A.; Banin, U.; Kadavanich, A. V.; Peng, X.; Alivisatos, A. P. Colloidal Chemical Synthesis and Characterization of InAs Nanocrystal Quantum Dots. *Appl. Phys. Lett.* **1996**, *69*, 1432–1434.
44. Aharoni, A.; Mokari, T.; Popov, I.; Banin, U. Synthesis of InAs/CdSe/ZnSe Core/Shell1/Shell2 Structures with Bright and Stable Near-Infrared Fluorescence. *J. Am. Chem. Soc.* **2006**, *128*, 257–264.
45. Banin, U.; Cao, Y.; Katz, D.; Millo, O. Identification of Atomic-Like Electronic States in Indium Arsenide Nanocrystal Quantum Dots. *Nature* **1999**, *400*, 542–544.
46. Zanolli, Z.; Pistol, M.-E.; Froberg, L. E.; Samuelson, L. Quantum-Confinement Effects in InAs−InP Core−Shell Nanowires. *J. Phys.: Condens. Matter* **2007**, *19*, 295219.
47. Nomura, S.; Kobayashi, T. Nonparabolicity of the Conduction Band in CdSe and CdS_xSe_{1-x} Semiconductor Microcrystallites. *Solid State Commun.* **1991**, *78*, 677–680.
48. Nishiguchi, N.; Yoh, K. Energy-Dependent Effective Mass Approximation in One-Dimensional Quantum Dots. *Jpn. J. Appl. Phys.* **1997**, *36*, 3928–3931.
49. Ekenberg, U. Enhancement of Nonparabolicity Effects in a Quantum Well. *Phys. Rev. B* **1987**, *36*, 6152–6155.
50. Wetzel, C.; Efros, Al. L.; Moll, A.; Meyer, B. K.; Omling, P.; Sobkowicz, P. Dependence on Quantum Confinement of the In-Plane Effective Mass in $Ga_{0.47}In_{0.53}As$/InP Quantum Wells. *Phys. Rev. B* **1992**, *45*, 14052–14056.
51. Hendorfer, G.; Seto, M.; Ruckser, H.; Jantsch, W.; Helm, M.; Brunthaler, G.; Jost, W.; Obloch, H.; Kohler, K. Enhancement of the In-Plane Effective Mass of Electron in Modulation-doped $In_xGa_{1-x}As$ Quantum Wells due to Confinement Effects. *Phys. Rev. B* **1993**, *48*, 2328–2334.
52. Chen, R.; Bajaj, K. K. Enhancement of the Electronic Effective Mass in Quantum Wires. *Phys. Rev. B* **1994**, *50*, 1949–1952.
53. Persson, M. P.; Xu, H. Q. Electronic Structure of Nanometer-Scale GaAs Whiskers. *Appl. Phys. Lett.* **2002**, *81*, 1309–1311.
54. Persson, M. P.; Xu, H. Q. Electronic Structure of 100-Orented Free-Standing Semiconductor Nanowires. *Nano Lett.* **2004**, *4*, 2409–2414.
55. Karanth, D.; Fu, H. Polarization Ratio and Effective Mass in InP Nanowires: Effect of Crystallographic Axis. *Phys. Rev. B* **2006**, *74*, 155312.
56. Lassen, B.; Willatzen, M.; Melnik, R.; Lew Yan Voon, L. C. Electronic Structure of Free-Standing InP and InAs Nanowires. *J. Mater. Res.* **2006**, *21*, 2927–2935.
57. Fu, H.; Wang, L.-W.; Zunger, A. Applicability of the k · p Method to the Electronic Structure of Quantum Dots. *Phys. Rev. B* **1998**, *57*, 9971–9987.
58. Madelung, O. *Semiconductors: Data Handbook*, 3rd ed.; Springer: Berlin, 2004.
59. Banin, U.; Lee, C. J.; Guzelian, A. A.; Kadavanich, A. V.; Alivisatos, A. P.; Jaskolski, W.; Bryant, G. W.; Efros, Al. L.; Rosen, M. Size-Dependent Electronic Level Structure of InAs Nanocrystal Quantum Dots: Test of Multiband Effective Mass Theory. *J. Chem. Phys.* **1998**, *109*, 2306–2309.
60. Wells, R. L.; Self, M. F.; Johansen, J. D.; Laske, J. A.; Aubuchon, S. R.; Jones, L. J. Tris(trimethylsilyl)Arsine and Lithium Bis(trimethylsilyl)Arsinide. *Inorg. Synth.* **1997**, *31*, 150–156.
61. Wang, F.; Tang, R.; Yu, H.; Gibbons, P. C.; Buhro, W. E. Size- and Shape-Controlled Synthesis of Bismuth Nanoparticles. *Chem. Mater.* **2008**, *20*, 3656–3662.
62. Peng, Z. A.; Peng, X. Nearly Monodisperse and Shape-Controlled CdSe Nanocrystals *via* Alternative Routes: Nucleation and Growth. *J. Am. Chem. Soc.* **2002**, *124*, 3343–3353.